Validation of Solar Radiation Surfaces from MODIS and Reanalysis Data over Topographically Complex Terrain

TODD A. SCHROEDER, ROBBIE HEMBER, AND NICHOLAS C. COOPS

Department of Forest Resources Management, University of British Columbia, Vancouver, British Columbia, Canada

SHUNLIN LIANG

Department of Geography, University of Maryland, College Park, College Park, Maryland

(Manuscript received 7 November 2008, in final form 24 June 2009)

ABSTRACT

The magnitude and distribution of incoming shortwave solar radiation (SW↓) has significant influence on the productive capacity of forest vegetation. Models that estimate forest productivity require accurate and spatially explicit radiation surfaces that resolve both long- and short-term temporal climatic patterns and that account for topographic variability of the land surface. This paper presents a validation of monthly average total (SW↓$_t$) and diffuse (SW↓$_{df}$) incoming solar radiation surfaces taken from North American Regional Reanalysis (NARR) data and Moderate Resolution Imaging Spectroradiometer (MODIS) satellite imagery for a mountainous region of the Pacific northwestern United States and Canada. A topographic solar radiation model based on a regionally defined clearness index was used to downscale the 32-km NARR SW↓$_t$ surfaces to 1 km, resulting in surfaces that better matched the spatial resolution of MODIS, as well as accounted for elevation and terrain effects including shadowing. Validation was carried out using a series of ground station measurements ($n = 304$) collected in 2003. The results indicated that annually, the NARR and MODIS SW↓$_t$ surfaces were both in strong agreement with ground measurements ($r = 0.98$ and 0.97), although the strength and bias of the relationships varied considerably by month. Correlations were highest in winter, early summer, and fall and lowest in spring. The NARR and MODIS SW↓$_{df}$ surfaces displayed poorer agreement with ground measurements ($r = 0.89$ and 0.79), the result of some months having negative correlations. The correlation and spatial structure between NARR and MODIS SW↓$_t$ surfaces was enhanced by topographic correction, resulting in more consistent input radiation surfaces for use in broad-scale forest productivity modeling.

1. Introduction

Incoming shortwave solar radiation (SW↓) is a key component of the surface energy balance, as well as a primary driver of forest productivity and plant growth. Several modeling frameworks exist from which to estimate forest productivity at various temporal and spatial scales (Cohen et al. 1996; Landsberg and Waring 1997; Thornton et al. 2002). Although the theory and application of these models differ, one similarity is the requirement of meteorological inputs including incoming solar radiation. As climate is an important driver of forest productivity, the reliability and precision of the predictions from these models relies heavily on the accuracy, resolution, and spatial extent of the meteorological inputs (Zhao et al. 2006). As many of these models are being used to study the potential impacts of climate change on forest production it is important that the meteorological inputs resolve both long- (e.g., mid-decadal oscillation) and short-term (e.g., daily and monthly average) patterns, provide seamless coverage across international borders, and suitably account for the finescale effects of land cover and topography.

In the Pacific Northwest (PNW) region of North America, significant improvements have been made to predicted surfaces of precipitation and temperature, including the development of temporally accurate, long-term normals (1961–91) and short-term monthly averages (2000–07) at 250-m gridcell resolutions (Hamann

Corresponding author address: Todd A. Schroeder, Forest Inventory and Analysis Program, USDA Forest Service, Rocky Mountain Research Station, Ogden, UT 84401.
E-mail: tschroeder@fs.fed.us

and Wang 2004; Wang et al. 2006). Conversely, forest productivity modelers have typically estimated incoming solar radiation using temperature and precipitation extremes (Coops et al. 2000; Thornton et al. 2000), coarse-resolution weather observations [e.g., National Aeronautics and Space Administration (NASA) Data Assimilation Office grids at $1° \times 1.25°$ gridcell resolution; see Running et al. 2004], or fine resolution (1-km gridcell resolution) surfaces averaged over relatively short time periods [e.g., Daily Surface Weather Data and Climatological Summaries (DAYMET) model, 1980–97; see Turner et al. 2004]. Significant progress has been made in developing methods to estimate SW↓ and photosynthetically active radiation (PAR) at fine spatial resolutions (1 km) using satellite reflectance data from the Moderate Resolution Imaging Spectroradiometer (MODIS) (Van Laake and Sanchez-Azofeifa 2004; Liang et al. 2006; Liu et al. 2008) and the Geostationary Operational Environment Satellite (GOES) (Perez et al. 2002; Zheng et al. 2008). These methods show great promise, however producing monthly average estimates requires intensive computations that have yet to be implemented on an operational basis. For North America, another source of radiation data that can resolve both long- and short-term patterns of SW↓ at relatively fine spatial resolutions comes from reanalysis datasets such as the North American Regional Reanalysis (NARR). NARR is an improved version of the National Centers for Environmental Prediction–National Center for Atmospheric Research (NCEP–NCAR) global reanalysis dataset.

The power of reanalyses lies within their consistent framework for collating in situ and remote sensing data into temporally and spatially discrete estimates of global climate forcings from land, ocean, and atmosphere. Although predictions from reanalyses are comprehensive in nature, the land surface products do have problems resulting from the assimilation of data taken primarily from atmospheric profiles (Sheffield et al. 2006) and forcing near-surface meteorology with model-based estimates of precipitation (Trenberth and Guillemot 1998; Serreze and Hurst 2000). These along with other sources of error tend to cause systematic biases in reanalysis predictions of incoming shortwave radiation (Betts et al. 1997; Sheffield et al. 2006). Based on field measurements, Betts et al. (1996) and Brotzge (2004) found that the NCEP–NCAR data consistently overestimated SW↓ by 17%–27%. Comparisons with satellite data have also revealed large positive biases in NCEP–NCAR SW↓ ranging from 25 to 50 W m^{-2} over the United States (Berbery et al. 1999) and from 40 to 80 W m^{-2} over Europe (Babst et al. 2008). In general, most studies attribute the overestimation of SW↓ to high transmissivity

in the NARR model atmosphere, resulting in insufficient atmospheric absorption and underestimation of cloud cover effects (Betts et al. 1996, 1997; Yang et al. 1999; Babst et al. 2008). One approach to removing bias in reanalysis data is by direct adjustment with ground measurements (Qian et al. 2006). This in effect rescales the reanalysis predictions to better match the seasonal and interannual variations observed at ground measurement stations.

After correcting for bias, the other major modulators of SW↓ include clouds, topography, and solar geometry (i.e., angle and elevation). In mountainous terrain, forcings from elevation, slope, aspect, and latitude all combine with cloud effects to form large gradients in SW↓ (Dubayah 1994). Slope and aspect combine seasonally with sun position to form shadows that reduce SW↓ in areas of rugged terrain. As elevation increases, the pathlength, or distance that SW↓ must traverse on its way to Earth, decreases. This elevation effect causes incoming direct radiation (SW↓$_{dr}$) to increase and incoming diffuse radiation (SW↓$_{df}$) to decrease with elevation. As vegetation directly responds to these gradients over various spatial and temporal scales, it is important that radiation surfaces used in forest productivity models properly account for these effects. Under partly cloudy conditions, the spatial variability in SW↓ is dominated by clouds, whereas under uniformly clear–cloudy conditions variability is regulated primarily by topography (Dubayah and Loechel 1997). Consequently, total incoming radiation (SW↓$_t$) at any one position on the landscape is the sum of SW↓$_{df}$ from the sky including clouds, SW↓$_{dr}$ from the sun, and SW↓$_{dr}$ and SW↓$_{df}$ reflected off of nearby terrain. A ''clearness index'' approach (Liu and Jordan 1960; Erbs et al. 1982; Oliveira et al. 2002) can be used to partition SW↓$_t$ surfaces into SW↓$_{dr}$ and SW↓$_{df}$ components. The vertical diffuse profile can be obtained by empirically scaling observed optical depth data according to a pressure-dependent lapse rate with elevation (Lowry 1980). Used in combination with a digital elevation model (DEM), the clearness index and the profiling method can provide estimates of SW↓$_{dr}$ and SW↓$_{df}$ on a horizontal surface at each elevation grid cell. Once partitioned, parameters representing the average solar day can be used to further correct for Earth–sun relationships, elevation, and topography, resulting in fully integrated estimates of SW↓$_t$ on a slope.

Although vegetation responds differently to direct and diffuse components of radiation (Gu et al. 2002; Brodersen et al. 2008), many satellite-driven forest productivity models [e.g., MODIS Product 17: Daily Photosynthesis/Annual Primary Production (GPP/NPP; Running et al. 2004); Physiological Principles Predicting Growth Using Satellite Data (3-PGS; Coops et al. 2000)]
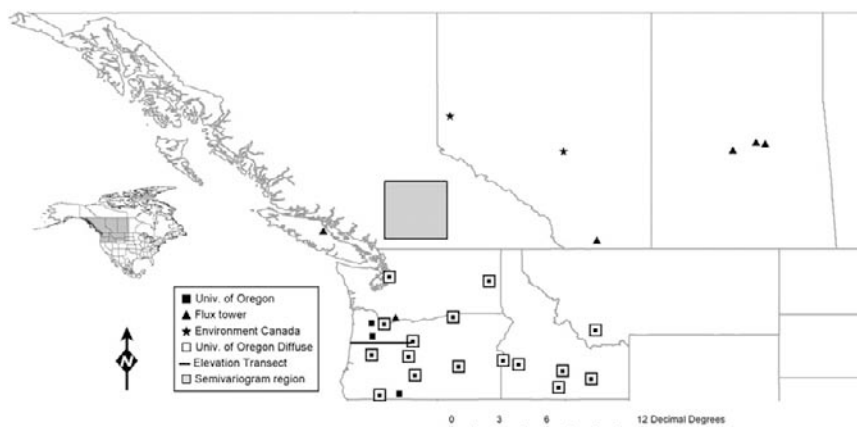
FIG. 1. Location of ground measurement stations, elevation transect, and semivariogram region within the PNW study area.

utilize only estimates of total PAR (typically converted from estimates of $SW\downarrow_t$). As satellite-based models advance to the point of accounting for these different types of radiation, a method that could accurately partition $SW\downarrow_t$ or PAR into its various components would have great merit. In this study, $SW\downarrow_{df}$ estimates are available from NARR via the clearness index and from MODIS via radiative transfer modeling (Liang et al. 2006). Given the spatial discord between ground observations and gridded radiation surfaces it is important to take a cautious approach when drawing conclusions from the direct comparison of the two. Nonetheless, ground observations provide one of the only available baselines from which to understand the uncertainty in predictions derived from each method.

The objective of this paper is to present a validation of $SW\downarrow_t$ and $SW\downarrow_{df}$ surfaces derived from NARR reanalysis data and from MODIS satellite imagery for a mountainous section of the PNW region of North America. As the MODIS $SW\downarrow_t$ surfaces are derived at a much higher spatial resolution (1 km), and with a more detailed radiative transfer methodology, we believe comparing MODIS with NARR will provide insight into the reliability of developing longer time series of radiation surfaces from NARR data. As the PNW region experiences distinct weather patterns that are heavily influenced by topography, we present the results on a monthly basis so as to explore seasonal trends in correlation and bias. As ground-based measurements of diffuse radiation are available, we briefly explore the accuracy of the $SW\downarrow_{df}$ surfaces derived by the NARR clearness index and MODIS radiative transfer methodologies. Since most pyranometers are leveled horizontally it is difficult to use ground data to understand the effect of elevation and topographic adjustments on the final $SW\downarrow$ surfaces. As a result, we use a transect

approach to more fully understand the value of the elevation correction. In addition, we directly compare the NARR and MODIS $SW\downarrow_t$ surfaces to gain insight into the impact of topographic correction.

The remainder of the paper is organized as follows: section 2 outlines the various spatial and ground-measured datasets. Section 3 presents a brief description of the major steps involved with processing the $SW\downarrow_t$ surfaces, including initial bias adjustment and topographic correction. In section 4, we validate the NARR and MODIS $SW\downarrow_t$ and $SW\downarrow_{df}$ surfaces using ground-measured pyranometer data. Validation is based on monthly correlations (Pearson r), biases (mean of predicted − mean of observed in watts per meter squared), and root-mean-square errors (RMSE; presented as a percentage of the mean estimate). As this comparison only validates the initial retrieval algorithm, we further explore the impact of elevation and topographic correction by presenting a direct comparison of the NARR and MODIS $SW\downarrow_t$ surfaces. Elevation effects are explored by examining the response of the $SW\downarrow$ surfaces over a mountainous elevation transect located in central Oregon. Semivariograms and monthly scatterplots are also used to further understand the effect of topographic correction on the incoming solar radiation surfaces. Section 5 discusses the validation results and potential implications of using the $SW\downarrow$ surfaces as inputs to forest productivity models.

2. Data

a. Ground data

The ground radiation data were collected at 27 stations located within the PNW study area (Fig. 1). The 27 stations comprised data collected from four different sources. The majority of sites ($n = 19$) were taken from

the University of Oregon's Solar Radiation Monitoring Laboratory (http://solardat.uoregon.edu/SolarData.html). Other data sources include Ameriflux ($n = 1$) (http://bwc.berkeley.edu/Amflux), Fluxnet-Canada ($n = 5$) (http://www.fluxnet-canada.ca), and Environment Canada ($n = 2$) (http://ec.gc.ca). All data were field recorded via pyranometers and were obtained as, or converted to, monthly average total incoming solar radiation in units of watts per meter squared (referred to as $SW{\downarrow}_t$). For 2003, a total of 304 (25 measurements per month, 2 sites had data for only 2 months) ground observations were available for validation of the NARR and MODIS $SW{\downarrow}_t$ surfaces. Of the 19 University of Oregon sites, 16 had coincident monthly average diffuse radiation measurements ($n = 184$, 15 per month, 1 site had data for only 4 months) in W m^{-2} (see Fig. 1 for locations, referred to as $SW{\downarrow}_{df}$). Although the ground measurements used for validation were collected with a variety of different pyranometers, studies have shown that uncertainty arising from instrument error is approximately 2.5% for total radiation and -9.1% for diffuse radiation (Vignola et al. 1996). Given the uncertainty already involved with comparing ground-measured radiation with gridded radiation surfaces we made no attempt to account for potential errors that might be associated with collecting radiation data with different instrument types.

The average elevation of the ground stations is 755 m above sea level (±480 m, min $= 7$ m, max $= 1560$ m). Although the study area encompasses a large elevation gradient (min $= 0$ m, max $= 4567$ m), nearly 52% of the DEM grid cells within the study area have an elevation at or below the average ground station elevation and 85% have an elevation at or below the maximum ground station elevation. Although the elevation of tree line varies, it is estimated to occur between 1500 and 2000 m in the Olympic Mountain range located within the study area. Therefore the ground stations (and subsequent validation) can be taken as a good representation of the radiation received at or below tree line elevation.

b. NARR SW↓

NARR $SW{\downarrow}_t$ surfaces for 2003 were downloaded in units of W m^{-2} from the North American Regional Reanalysis Web site (http://www.cdc.noaa.gov). Derived at 32-km resolution every 3 h (presented here as monthly averages), NARR climatologies are derived using the standard meteorological forecasting algorithm referred to as the eta model (Black 1994). Briefly, the surface radiation balance (e.g., incoming and outgoing shortwave and longwave) is estimated by the model using a precipitation assimilation procedure (Zhao et al. 1997), adjusting ambient conditions to more closely match observed precipitation measurements from gauge, ra-

dar, and satellite data. NARR is based on a modified version of the Eta Model, originally used in the National Centers for Environmental Prediction–National Center for Atmospheric Research global reanalysis (Kalnay et al. 1996; Kistler et al. 2001). Model changes include an increase in horizontal and vertical resolution, as well as incorporation of an improved 3D variational data assimilation system (3DVAR; Mittelstadt 1998). Currently, NARR data (including $SW{\downarrow}_t$ surfaces) are available for the entire North American continent from 1979 to present. From this point forward we use NARR to refer to the radiation surface data after bias adjustment (described in section 3a), whereas "original NARR" refers to the data as they were obtained directly from the above Web site.

c. MODIS SW↓

MODIS $SW{\downarrow}_t$ surfaces for 2003 were produced by the University of Maryland's Department of Geography. The 1-km resolution surfaces were received in units of monthly average PAR (i.e., total incoming radiation in the 400–700-nm spectral range) in kilojoules per meter squared per day. The PAR surfaces were originally created from MODIS spectral data using the processing methodology outlined in Liang et al. (2006). Briefly, there are two steps in deriving instantaneous PAR (both direct and diffuse components) from MODIS imagery. First, the surface reflectance from the "clearest" observation in a temporal window is determined for each pixel in the satellite image. The second step is to convert the determined surface reflectance to estimates of incident PAR using a lookup table approach. Based on radiative transfer theory, this method differs from others as surface reflectance and atmospheric properties (e.g., optical depth) are simultaneously estimated from the satellite imagery. A simple linear regression model was used to predict daily average PAR from the instantaneous MODIS estimates generated from both *Terra* (images acquired in morning) and *Aqua* (images acquired in afternoon) satellites. Monthly average values were then calculated from the daily integrated estimates. Before conversion to $SW{\downarrow}_t$ (discussed under bias correction below) the MODIS PAR surfaces (both direct and diffuse components) were converted from kilojoules per meter squared per day to watts per meter squared.

d. Other GIS inputs

The topographic solar radiation model (outlined in Fig. 2) requires several spatial inputs, most of which are derived directly from a DEM. Here we use a radar derived DEM acquired in February 2000 as part of the Shuttle Radar Topography Mission (SRTM).
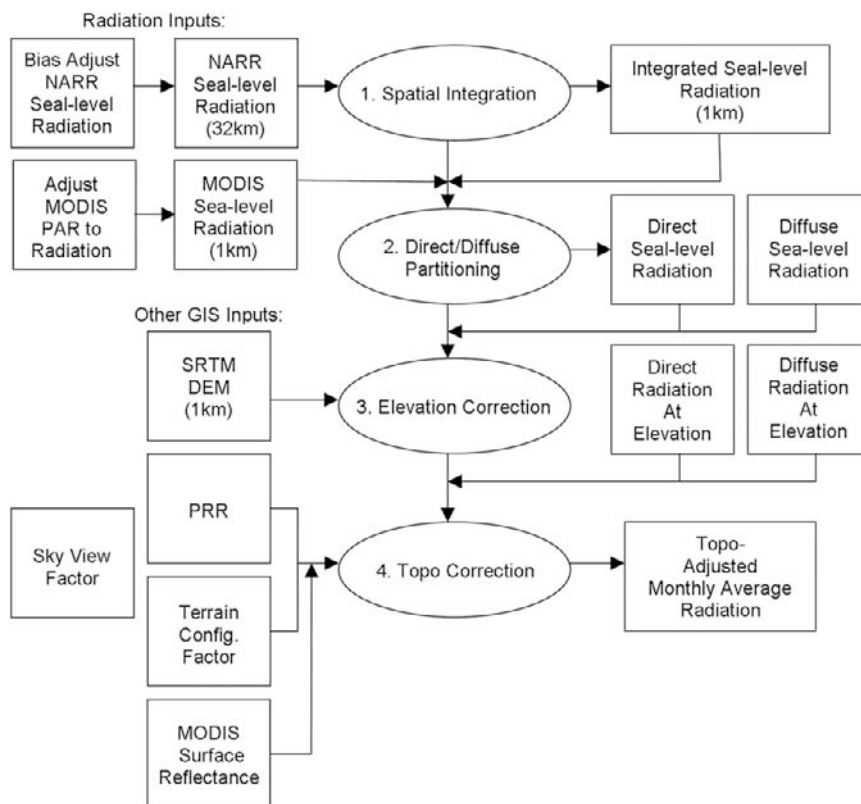
FIG. 2. Topographic solar radiation model (adapted from Dubayah and Loechel 1997).

SRTM DEM data were obtained at 90-m gridcell resolution from the Consultative Group for International Agriculture Research—Consortium for Spatial Information (CGIAR-CSI; http://srtm.csi.cgiar.org/). Based on the "unfinished" 3 arc-s data originally released by NASA, the CGIAR-CSI SRTM version-3 data have been hydrologically corrected with a gap-filling algorithm to remove no-data regions. Areas of no data were interpolated with auxiliary DEMs [e.g., National Elevation Data (NED) and global digital elevation model 30 arc-s topography database (GTOPO30)] to produce a smooth, continuous surface. The CGIAR-CSI SRTM DEM version-3 data (referred to hereinafter as DEM) for the PNW study area were downloaded as separate $1° \times 1°$ tiles, then seamlessly stitched together using the "mosaic" command in Arcinfo Grid.

Once assembled, the 90-m DEM was resampled to 1 km (using nearest-neighbor resampling) and used to create three additional variables required by the topographic solar radiation model. The skyview factor V_d, which is used to correct the partitioned diffuse radiation component, is an integrated estimate of the total amount of unobstructed sky visible on a slope in 16 view angle directions (1 = unobstructed, 0 = completely obstructed; Dubayah and van Katwijk 1992). The terrain

configuration factor C_t, which is used to account for reflected radiation from nearby terrain, is an estimate of the surrounding terrain visible to a position on the land surface (1 = only terrain visible, 0 = only sky visible; Dubayah and van Katwijk 1992). Both V_d and C_t were derived using the Linux version of the Image Processing Workbench (IPW; Frew 1991). Potential relative radiation (PRR) is a relative estimate of the effect of solar orientation caused by local topography (e.g., shadowing; Pierce et al. 2005). To estimate the effects of monthly Earth–sun movements, the day closest to the average solar period for each month (i.e., monthly average solar day) was used along with hourly specific solar azimuth and inclination angles to produce a series of hillshade surfaces in Arcinfo Grid. These hillshade surfaces were summed to form "potential" relative radiation surfaces for each month (analogous to integrated monthly average cosine of the illumination angle). As the relative values of the monthly PRR surfaces are unbounded, the highest value in each grid represents the location that receives the highest amount of surface radiation in the absence of clouds. Each monthly surface was divided by its maximum value to form a relative index ranging from 0 (no radiation) to 1 (maximum potential radiation). The monthly indexed PRR surfaces were used to modify the

amount of partitioned direct radiation received at the land surface due to shadowing (i.e., PRR × SW↓$_{dr}$).

The topographic solar radiation model also requires monthly estimates of terrain reflectance or albedo, which when used in conjunction with C_t, yield estimates of the amount of radiation reflected off nearby terrain. Similar to Dubayah and Loechel (1997), we estimate albedo using red surface reflectance (spectral range of 620–670 nm), taken here from the MODIS vegetation indices monthly L3 global 1-km product. Though the use of broadband albedo surfaces from MODIS would be preferred, tests indicated that within the PNW region red surface reflectance was a near-linear proxy for visible albedo ($r = 0.95$) and a strong ($r = 0.82$) but nonlinear predictor of broadband albedo (including shortwave infrared region). Although the nonlinear trend likely resulted in a slight underestimation of broadband albedo, we feel our conservative use of red surface reflectance had minimal impact on the final results, especially given the relatively small contribution of reflected radiation to SW↓$_t$. Additional use of spatial inputs within the topographic solar radiation model will be discussed in more detail in section 3b.

3. Processing SW↓ surfaces

a. Initial bias adjustment

Since the literature indicates it is likely that SW↓$_t$ surfaces taken from reanalysis data have substantial bias, we opted to correct for this prior to performing topographic correction. A leave-one-out, cross-validated, reduced-major-axis regression [RMA regression; for details see Cohen et al. (2003)] model (slope = 0.91, intercept = −18.66) was developed across months to adjust for the bias observed in the original NARR SW↓$_t$ surfaces. The same regression modeling approach was also used to convert the MODIS PAR total (slope = 1.87, intercept = 12.67) and diffuse (slope = 1.10, intercept = 15.03) surfaces to units of SW↓ (W m^{-2}). This regression approach effectively calibrated both the NARR and MODIS SW↓ surfaces to the same ground data, allowing robust cross comparison of model errors in similar units. Although incident PAR is often assumed to be half of incident shortwave radiation (Meek et al. 1984), the direct conversion of MODIS PAR to SW↓ with the regression approach eliminated the need to use a fixed ratio, which can vary across space and time (Alados et al. 1996).

b. Topographic solar radiation model

After initial bias adjustment both the NARR and MODIS SW↓$_t$ surfaces were corrected for topographic effects using a topographic solar radiation model based on work by Dozier (1980, 1989), Dozier and Frew (1990), and presented by Dubayah and Loechel (1997). As the nuances of the topographic model have been previously described (see Dubayah 1992, 1994; Dubayah and Rich 1995) we present only the major steps involved, with primary emphasis placed on highlighting the small changes made to adapt the original model (developed to correct instantaneous SW↓$_t$ surfaces) to monthly average surfaces. The four major modeling steps that compose the topographic solar radiation model are presented in Fig. 2.

1) SPATIAL INTEGRATION

The 32-km NARR surfaces were first resampled to 1-km gridcell resolution using nearest-neighbor resampling, then smoothed by taking the mean of a 32 × 32 rectangular moving window. This mean smoothing procedure acted to minimize errors in the spatial alignment of the SW↓$_t$ surfaces and the DEM and also served to remove the imprint of the larger 32-km grid cell from the final predicted SW↓$_t$ surfaces. The MODIS SW↓$_t$ surfaces were not resampled or smoothed as the data were originally created at the 1-km gridcell resolution.

2) DIRECT–DIFFUSE PARTITIONING

The three sources of radiation received on a slope include direct radiation from the sun, diffuse radiation from obstructed sky, and diffuse and direct radiation reflected from surrounding terrain features. To account for the effects of terrain on each of these sources of radiation requires partitioning SW↓$_t$ surfaces into SW↓$_{dr}$ and SW↓$_{df}$. To estimate the fraction of diffuse radiation from SW↓$_t$ (i.e., SW↓$_{df}$/SW↓$_t$) we used a clearness index K_T approach (Liu and Jordan 1960; Katsoulis 1991; Erbs et al. 1982; Oliveira et al. 2002):

$$K_T = \frac{SW\downarrow_t}{S_0}, \qquad (1)$$

where SW↓$_t$ is the total incoming shortwave solar radiation represented here by the NARR SW↓$_t$ surfaces, S_0 is the monthly average exoatmospheric irradiance on a horizontal surface, and K_T is the clearness index representing the total transmittance T of the atmosphere on a monthly average basis. Surfaces of monthly average S_0 assuming a solar constant of 1368 W m^{-2} were developed in units of megajoules per meter squared per day for daylight hours using Eq. (2) (Sellers 1965; Duffie and Beckman 1974),

$$S_0 = 37.210 \left(\frac{\bar{d}}{d}\right)^2 (h \sin\phi \sin\delta + \cos\phi \cos\delta \cos h), \qquad (2)$$

where $(\bar{d}/d)^2$ is the monthly average Earth–sun distance, h is the monthly average sunset hour angle in radians
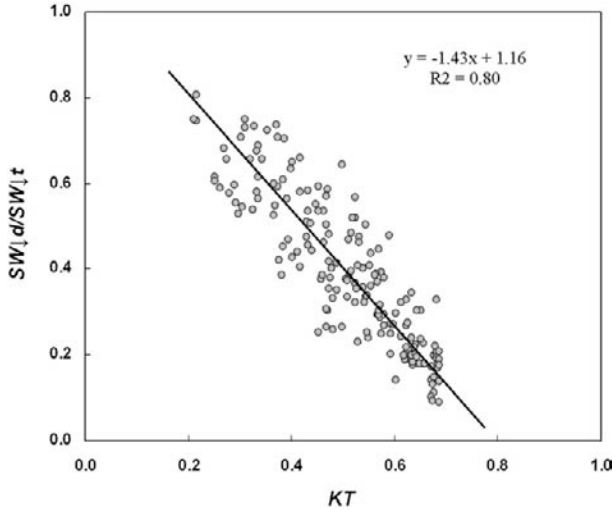
FIG. 3. PNW clearness index (K_t) equation used to estimate the fraction of diffuse radiation (SW$\downarrow_{df}$/SW$\downarrow_t$) from the NARR and MODIS total incoming solar radiation surfaces.

[defined as $h = \arccos(-\tan\phi \tan\delta)$], ϕ is the latitude in radians, and δ is the monthly average declination angle in radians. Once completed, the monthly average S_0 surfaces were converted to watts per meter squared and combined with the NARR SW$\downarrow_t$ surfaces to obtain K_T.

Other equations have been developed to estimate SW$\downarrow_{df}$/SW$\downarrow_t$ from K_T, however they are generally not as effective when applied outside the region they were initially developed for (LeBaron and Dirmhirn 1983). As ground-measured direct and diffuse radiation was available from station measurements ($n = 184$), we developed a regionally specific equation (Fig. 3; slope = −1.43, intercept = 1.16, $r^2 = 0.80$) to predict SW$\downarrow_{df}$/SW$\downarrow_t$ from K_T. Although the clearness index equation (K_T) was developed using the NARR SW$\downarrow_t$ surfaces, it was also used to partition the MODIS SW$\downarrow_t$ surfaces for input into the elevation correction portion of the topographic solar radiation model. By using the NARR-derived K_T for MODIS partitioning we were better able to compare the effect of the topographic correction by reducing unwanted variance associated with applying a separate MODIS-derived K_T. We note that when performing validation with ground data we use the MODIS SW$\downarrow_{df}$ surfaces derived via the radiative transfer modeling approach described earlier in section 2c. Finally, the diffuse component (SW$\downarrow_{df}$) was obtained by multiplying SW$\downarrow_{df}$/SW$\downarrow_t$ by SW$\downarrow_t$, and the direct component (SW$\downarrow_{dr}$) by subtracting SW$\downarrow_{df}$ from SW$\downarrow_t$.

3) ELEVATION CORRECTION

Since elevation effects are only broadly considered (i.e., at the 32-km resolution) in the NARR forecast-ing algorithm and are not explicitly considered in the MODIS PAR algorithm, SW$\downarrow_t$ surfaces developed by both methods were assumed to represent conditions at sea level. As elevation increases, the amount of diffuse radiation received at the surface decreases and the amount of direct radiation increases because of a decrease in pathlength. To correct the SW$\downarrow_{dr}$ and SW$\downarrow_{df}$ surfaces for elevation effects requires an estimate of optical depth t_0, which can be taken from its relationship with total transmittance T, $T = e^{-t_0}$. As we assume t_0 to represent sea level conditions, we obtain optical depth at the height of each elevation grid cell (t_z) through the use of the lapse rate in atmospheric pressure (Dubayah and van Katwijk 1992),

$$t_z = t_0 \left(\frac{P_{\text{height}}}{P_{\text{sealevel}}} \right), \tag{3}$$

where t_0 is the optical depth at sea level estimated as $-\ln T$ [T is taken from K_T in Eq. (1)], P_{height} is air pressure at the elevation of each DEM grid cell in bars, and P_{sealevel} is the air pressure at sea level in bars. Air pressure was derived for each DEM grid cell using a second-order polynomial equation ($0.000\,000\,005x^2 - 0.0001x + 1.0128$; x = DEM elevation in meters) based on the *U.S. Standard Atmosphere, 1976* (COESA 1976).

After estimating t_0 and t_z, the profiling method originally formulated by Lowry (1980) and modified by Dubayah and van Katwijk (1992) was used to estimate the diffuse radiation received on a horizontal surface at the elevation of each DEM grid cell (SW$\downarrow_{dfe}$),

$$SW\downarrow_{dfe} = SW\downarrow_{df} \left(\frac{M_z - e^{-t_z/\cos\theta_0}}{M_0 - e^{-t_o/\cos\theta_0}} \right), \tag{4}$$

where SW$\downarrow_{df}$ is the diffuse component partitioned from the SW$\downarrow_t$ surfaces in Eq. (1) (assumed to be at sea level), t_z and t_0 are optical depths at height and reference level (i.e., sea level), $\cos\theta_0$ is the monthly averaged daytime cosine of the solar zenith angle [this is a generalization implemented for monthly data; see Eq. (7) below], and M_z and M_0 are terms estimating the fraction of unabsorbed exoatmospheric flux at height and reference level derived by Lowry (1980),

$$M_j = (1 - 0.027e^{2P_j/P_0}) \left[1.075 - 0.105 \ln\left(\frac{1}{\cos\theta_0} \right) \right], \tag{5}$$

where P_0 and P_j are atmospheric pressure at sea level and height j.

The direct radiation received on a horizontal surface at the elevation of each DEM grid cell (SW$\downarrow_{dre}$) was estimated by
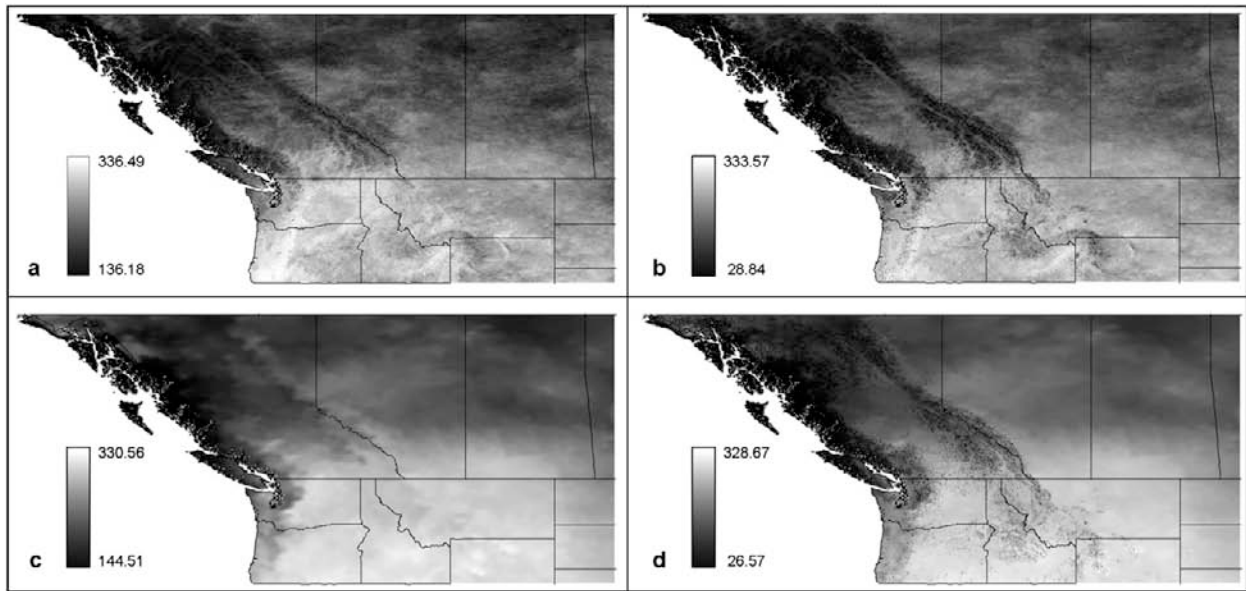
FIG. 4. July 2003 monthly average total incoming solar radiation (W m^{-2}) for (a) MODIS SW$\downarrow_{te}$, (b) MODIS SW$\downarrow_{tet}$, (c) NARR SW$\downarrow_{te}$, and (d) NARR SW$\downarrow_{tet}$.

$$SW\downarrow_{dre} = S_0 e^{-t_z/\cos\theta_0}, \qquad (6)$$

where $\cos\theta_0$ is a grid representing the monthly averaged daytime cosine of the solar zenith angle derived by Gupta et al. (2001),

$$\cos\theta_0 = \frac{\{f\cos^{-1}(-f/g) + g[1-(f/g)^2]^{1/2}\}}{\cos^{-1}(-f/g)}, \qquad (7)$$

where $f = \sin(\phi)\sin(\delta)$ and $g = \cos(\phi)\cos(\delta)$. Total radiation received on a horizontal surface at the elevation of each DEM grid cell (SW$\downarrow_{te}$) was then obtained by adding the SW$\downarrow_{dfe}$ and SW$\downarrow_{dre}$ components. Equations (3)–(7) were implemented in Arcinfo Grid to produce the NARR and MODIS SW$\downarrow_{te}$, SW$\downarrow_{dfe}$, and SW$\downarrow_{dre}$ surfaces.

4) TOPOGRAPHIC CORRECTION

Once partitioned and adjusted for elevation effects, the NARR and MODIS SW$\downarrow$ surfaces were corrected for topographic effects. Topographically corrected diffuse radiation (SW$\downarrow_{dfet}$) was obtained for each grid cell by

$$SW\downarrow_{dfet} = SW\downarrow_{dfe} V_d, \qquad (8)$$

where V_d is the skyview factor. To account for sun illumination and shadowing effects, the direct radiation received on a slope at the elevation of each grid cell (SW$\downarrow_{dret}$) was obtained by

$$SW\downarrow_{dret} = SW\downarrow_{dfe} PRR, \qquad (9)$$

where PRR is the potential relative radiation index (see section 2d for more information on PRR). The amount of radiation reflected (SW$\uparrow_{ref}$) off of surrounding terrain was estimated by

$$SW\uparrow_{ref} = C_t \overline{R}_{mod}[SW\downarrow_{dfe}(1 - V_d) + SW\downarrow_{dre}PRR], \qquad (10)$$

where C_t is the terrain configuration factor (see section 2d for more information on C_t) and $\overline{R}_{mod}$ is the monthly average MODIS red surface reflectance mean smoothed with a 32 km $\times$ 32 km rectangular moving window. Total incoming radiation on a slope (SW$\downarrow_{tet}$) was obtained as the sum of the three components given above,

$$SW\downarrow_{tet} = SW\downarrow_{dfet} + SW\downarrow_{dret} + SW\downarrow_{ref}. \qquad (11)$$

For more information regarding the theoretical justification and implementation of the topographic corrections applied here see Dubayah and Loechel (1997). An example of the NARR and MODIS July 2003 total incoming shortwave solar radiation surfaces before (i.e., SW$\downarrow_{te}$) and after (SW$\downarrow_{tet}$) topographic corrections is shown in Figs. 4a–d.

4. Validation of SW$\downarrow$ surfaces

a. Monthly average total incoming shortwave radiation (SW$\downarrow_t$)

After initial bias adjustment but prior to elevation and topographic correction, the NARR and MODIS SW$\downarrow_t$
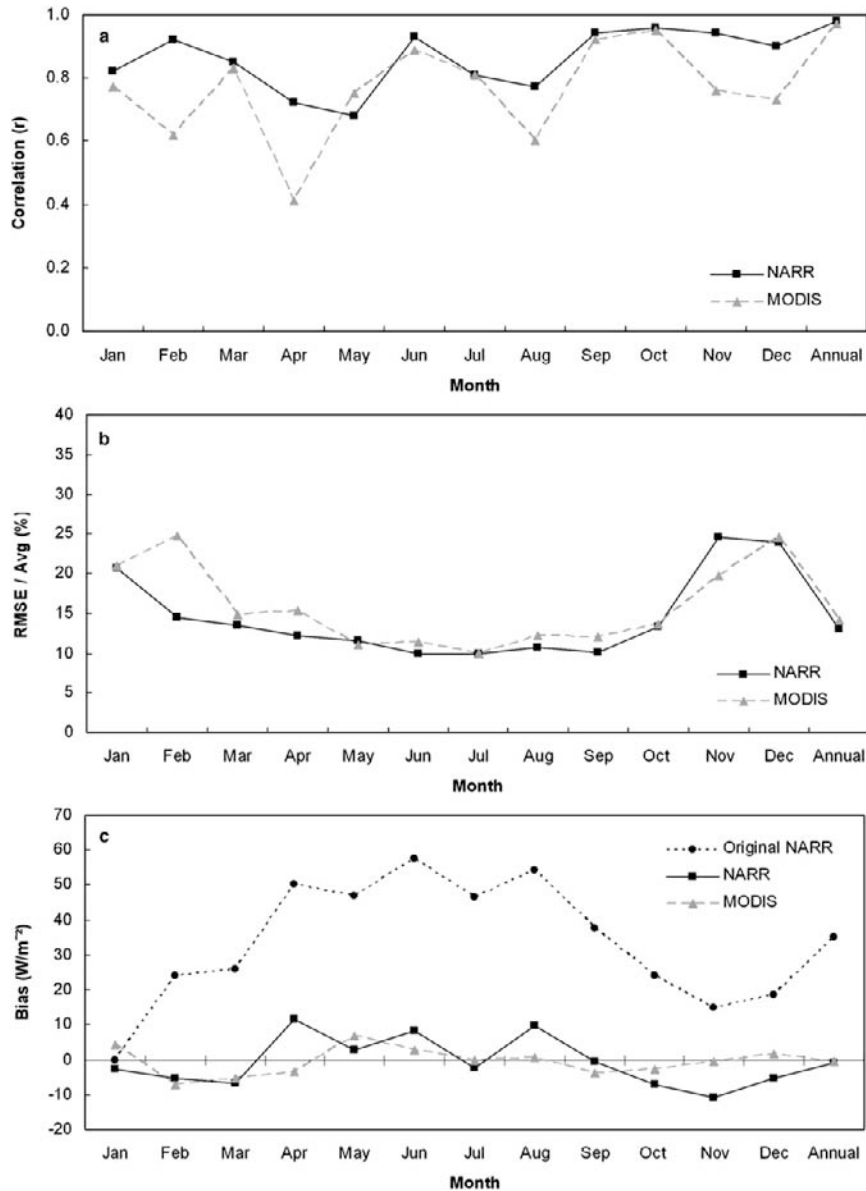
FIG. 5. (a) Correlation (r), (b) (RMSE/average) $\times$ 100 (%), and (c) bias (W m^{-2}) based on comparison of ground-measured monthly average total incoming solar radiation and original NARR (bias only), NARR, and MODIS SW$\downarrow_t$ surfaces.

surfaces were compared with ground-measured total incoming radiation recorded in 2003 ($n = 304$) (see Fig. 1 for station locations). To minimize the spatial discrepancy between ground and gridded radiation surfaces the radiation values were extracted from the SW$\downarrow_t$ surfaces using the mean of the 3 $\times$ 3 window centered on the spatial coordinate of each ground station. On an annual basis, both the NARR and MODIS SW$\downarrow_t$ surfaces were in strong agreement with ground-measured radiation data (Fig. 5a; $r = 0.98$ and 0.97, respectively). On a monthly basis, however, the correlation between the SW$\downarrow_t$ sur-

faces and the ground-measured radiation data was much more variable (Fig. 5a). Both the NARR and MODIS SW$\downarrow_t$ surfaces had the highest correlations with ground-measured data in October ($r = 0.96$ and 0.95, respectively) and the lowest in the spring months of April (MODIS; $r = 0.41$) and May (NARR; $r = 0.68$). The NARR SW$\downarrow_t$ surfaces had correlations of 0.80 or higher in 9 months and the MODIS SW$\downarrow_t$ surfaces in 5 of the 12 months in 2003.

Root-mean-square error reported as a percentage of the mean estimate [(RMSE/average) $\times$ 100] is shown in Fig. 5b. On an annual basis, both the NARR and MODIS
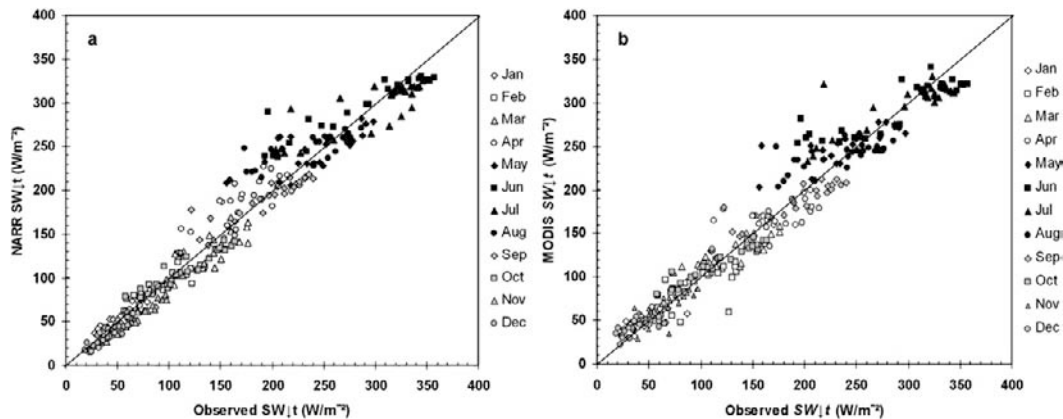
FIG. 6. Observed (from ground measurements) vs predicted monthly average total incoming solar radiation from (a) NARR SW$\downarrow_t$ surfaces and (b) MODIS SW$\downarrow_t$ surfaces.

SW$\downarrow_t$ surfaces had similar error (12.93% and 14.22%, respectively). For the NARR SW$\downarrow_t$ surfaces the monthly errors ranged from a high of 24.53% in November to a low of 9.90% in July. Similarly the MODIS SW$\downarrow_t$ surfaces also had the lowest error in July (9.88%) but had the highest error relative to the mean in February (24.79%). Overall, the NARR and MODIS SW$\downarrow_t$ surfaces showed very similar seasonal patterns of error, with both tending to have less error in late spring, summer, and early fall, and the most error in winter and late fall.

Prior to initial bias adjustment, the original NARR SW$\downarrow_t$ surfaces were found to have substantial bias. Annually, the original NARR SW$\downarrow_t$ surfaces were an average of 35.13 W m^{-2} greater than the ground-measured radiation data (Fig. 5c). The initial bias adjustment, however, successfully reduced the annual bias in the NARR SW$\downarrow_t$ surfaces to an average of 0.76 W m^{-2} less than the ground-measured radiation data (Fig. 5c). The maximum bias observed in the NARR SW$\downarrow_t$ surfaces was in April (11.66 W m^{-2}) and the minimum in November (−10.91 W m^{-2}). The NARR SW$\downarrow_t$ surfaces were observed to have slightly negative ($\geq$−10.00 W m^{-2}) bias statistics in winter months (e.g., December, January, February) and slightly positive ($\leq$10.00 W m^{-2}) bias statistics in spring and summer months (e.g., April, May, June, August). Annually, the MODIS SW$\downarrow_t$ surfaces were an average of 0.54 W m^{-2} less than the ground-measured radiation data (Fig. 5c). The maximum bias was observed in May (6.98 W m^{-2}) and the minimum in February (−7.24 W m^{-2}). The MODIS SW$\downarrow_t$ surfaces were observed to have less bias than the NARR SW$\downarrow_t$ surfaces in 8 of the 12 months in 2003. The relationship between observed (from ground measurements) and predicted (from NARR and MODIS SW$\downarrow_t$ surfaces) monthly average total incoming solar radiation is shown in Figs. 6a and 6b.

b. Monthly average diffuse radiation (SW$\downarrow_{df}$)

The NARR and MODIS SW$\downarrow_{df}$ surfaces were compared with field measured monthly average diffuse radiation recorded in 2003 at 16 field sites ($n = 184$). The NARR SW$\downarrow_{df}$ surfaces were derived via the clearness index approach (see Fig. 3 for equation) while the MODIS SW$\downarrow_{df}$ surfaces were taken directly from the radiative transfer model of Liang et al. (2006). On an annual basis, both the NARR and MODIS SW$\downarrow_{df}$ surfaces were found to be in relatively good agreement with the ground-measured radiation data (Fig. 7a; $r = 0.89$ and 0.79, respectively). However, on a monthly basis, the observed correlations between the SW$\downarrow_{df}$ surfaces and the ground-measured diffuse radiation data were highly variable (Fig. 7a). Both the NARR and MODIS SW$\downarrow_{df}$ surfaces had the highest correlations with ground-measured data in January ($r = 0.81$ and 0.86, respectively), and the lowest in March (NARR; $r = −0.10$) and September (MODIS; $r = −0.34$). The NARR SW$\downarrow_{df}$ had correlations of 0.45 or higher in 8 months and the MODIS SW$\downarrow_t$ surfaces in 3 of the 12 months tested in 2003. Overall, the correlations were generally weak, with the MODIS SW$\downarrow_{df}$ surfaces having negative correlations in 4 months and the NARR SW$\downarrow_{df}$ surfaces in 2 of the 12 months in 2003.

Error in the predicted SW$\downarrow_{df}$ surfaces, reported as a percentage of the mean estimate [(RMSE/average) $\times$ 100], is presented in Fig. 7b. On an annual basis, the NARR SW$\downarrow_{df}$ surfaces had slightly less error than the MODIS SW$\downarrow_{df}$ surfaces (20.99% and 27.42%, respectively). For the NARR SW$\downarrow_{df}$ surfaces the monthly errors ranged from a high of 28.00% in July to a low of 10.44% in October. The MODIS SW$\downarrow_{df}$ surfaces also had the highest error in July (34.92%) but had the lowest error relative to the mean in November (12.19%). Both the
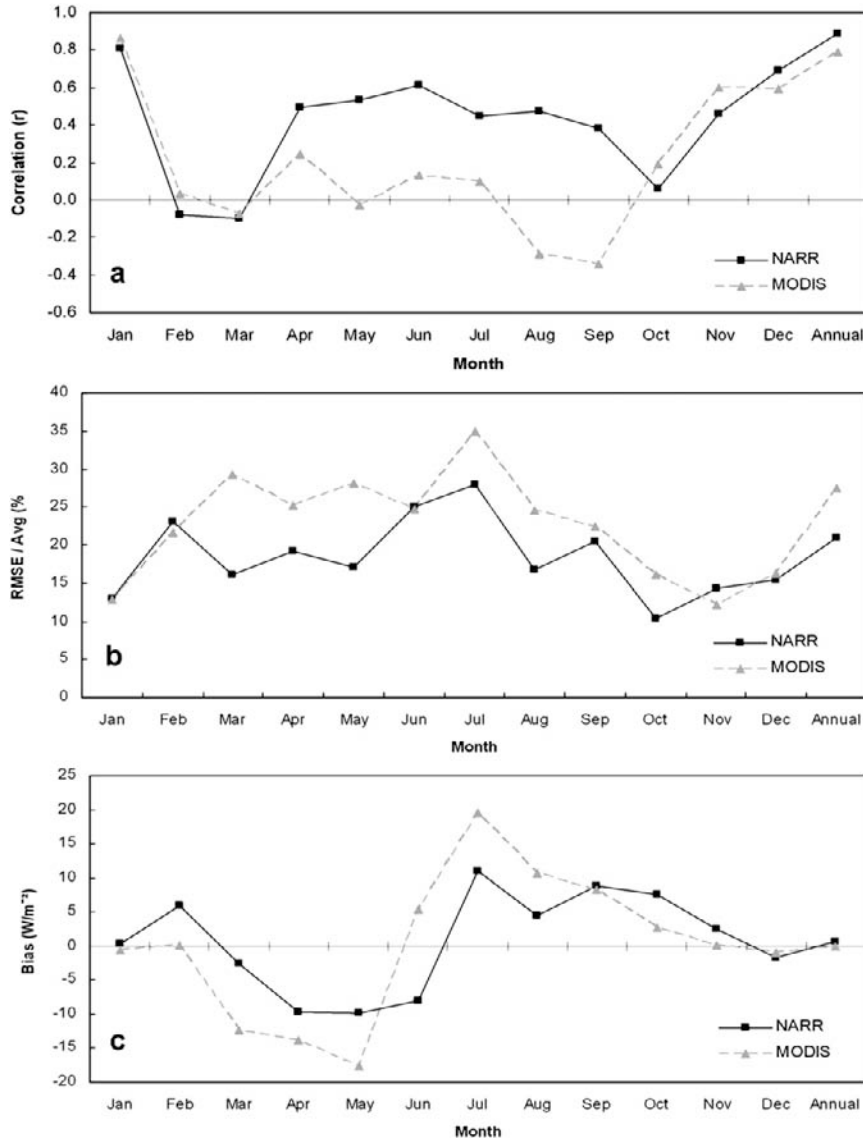
FIG. 7. As in Fig. 5, but for ground-measured monthly average diffuse solar radiation and
NARR and MODIS SW$\downarrow_{df}$ surfaces.

NARR and MODIS SW$\downarrow_{df}$ surfaces displayed highly variable patterns of monthly error. The NARR SW$\downarrow_{df}$ surfaces had less error than the MODIS SW$\downarrow_{df}$ surfaces in 8 of the 12 months tested in 2003.

Annually the NARR SW$\downarrow_{df}$ surfaces were an average of 0.73 W m^{-2} greater than the ground-measured diffuse radiation data recorded in 2003 (Fig. 7c). The low annual bias was the result of having some months with strong negative and some months with strong positive biases. The maximum bias was observed in July (11.09 W m^{-2}) and the minimum in May (-9.85 W m^{-2}). Annually the MODIS SW$\downarrow_{df}$ surfaces showed no bias when compared with the ground-measured diffuse radiation data. Similar to the NARR SW$\downarrow_{df}$ surfaces,

the lack of annual bias resulted from some months having strong negative and some months having strong positive biases (Fig. 7c). Resembling the NARR SW$\downarrow_{df}$ surfaces, the maximum bias in MODIS SW$\downarrow_{df}$ was in July (19.50 W m^{-2}) and the minimum in May (-17.70 W m^{-2}). Both the NARR and MODIS SW$\downarrow_{df}$ surfaces showed very similar seasonal variations, with negative (≥ -20.00 W m^{-2}) biases in spring (e.g., March, April, May) and positive (≤ 20.00 W m^{-2}) biases in summer and early fall (e.g., July, August, September, October). The relationship between observed (from ground measurements) and predicted (from NARR and MODIS SW$\downarrow_{df}$ surfaces) monthly average diffuse solar radiation is shown in Figs. 8a and 8b.
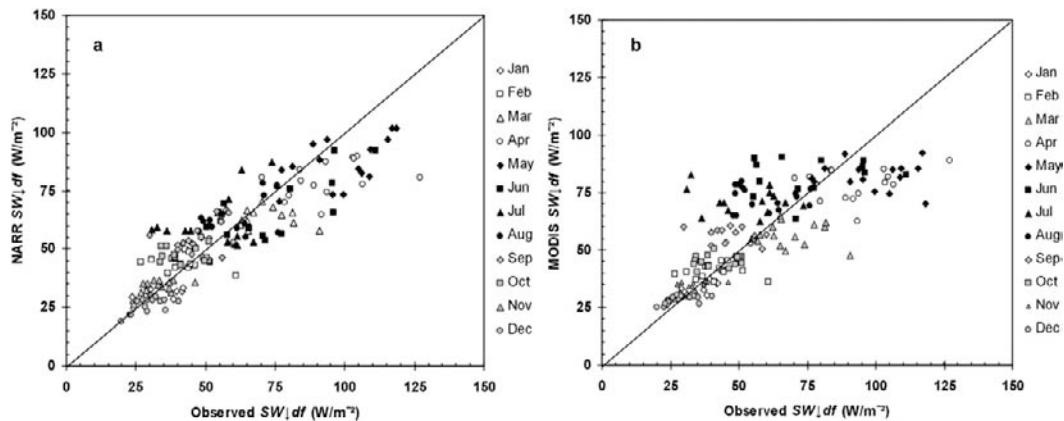
FIG. 8. Observed (from ground measurements) vs predicted monthly average diffuse solar radiation from (a) NARR SW↓$_{df}$ surfaces based on regional K_t equation and (b) MODIS SW↓$_{df}$ surfaces based on radiative transfer methodology.

c. Elevation correction

Although the 27 measurement stations are all located at different elevations, there was no evidence that ground-measured total incoming radiation (the majority of which is direct radiation) increased, or diffuse radiation decreased, with increasing elevation. As a result, the elevation correction could not be expected to improve the observed versus predicted relationships between the

ground-measured and satellite-derived radiation shown in Figs. 6 and 8. Therefore, an alternative approach was employed to improve our understanding of how the SW↓ surfaces changed with elevation. A 230-km transect located in a mountainous section of central Oregon (see Fig. 1 for location) was used to derive profiles of NARR and MODIS direct, diffuse, and total incoming radiation. Transects were derived for SW↓ surfaces both before [i.e., SW↓$_t$, SW↓$_{df}$, and SW↓$_{dr}$ surfaces output from
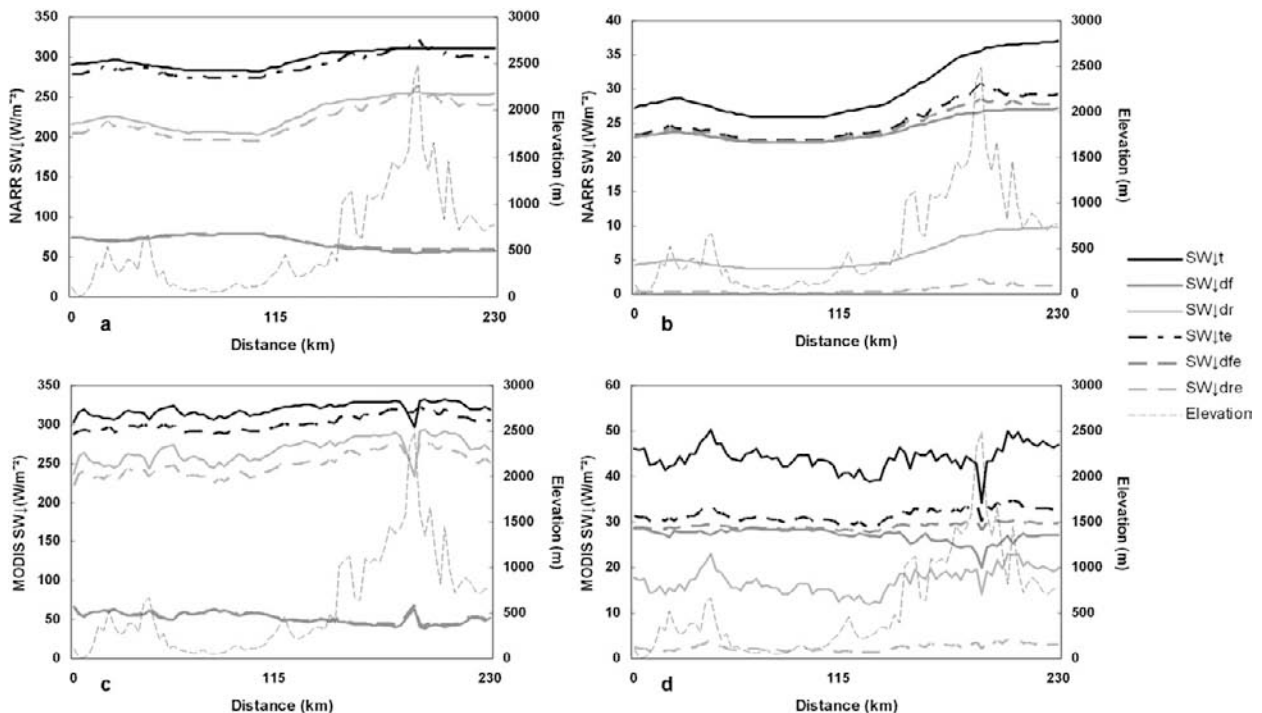

FIG. 9. Response of solar radiation surfaces to changes in elevation along a 230-km transect in central Oregon (see Fig. 1 for transect location). Profiles are for (a) NARR July radiation, (b) NARR December radiation, (c) MODIS July radiation, and (d) MODIS December radiation. Transect distance: 0 km = west, 230 km = east.

direct–diffuse partitioning in section 3b(2)] and after elevation correction [i.e., SW$\downarrow_{te}$, SW$\downarrow_{dfe}$, and SW$\downarrow_{dre}$ surfaces output from elevation correction in section 3b(3)].

The profiles in Fig. 9 show that the NARR SW$\downarrow$ surfaces noticeably respond to changes in elevation even before the elevation corrections were applied (solid lines in Figs. 9a,b). The July NARR radiation profile (Fig. 9a) shows that the elevation correction correctly assigns the highest radiation value to the top of the highest peak (at approximately 200 m on the transect) and lowers all other values as elevation decreases. The SW$\downarrow_t$ in July does not change considerably after elevation correction, largely because summer radiation is primarily driven by direct radiation, which is relatively unaffected by the elevation correction. In the NARR December profile however, diffuse radiation is the primary driver of total radiation. Because winter transmittance T is low, the direct component drops considerably as the result of the elevation correction applied in Eq. (6). This leads to a considerable drop in SW$\downarrow_{te}$ after the elevation corrections are applied.

Prior to elevation correction, the MODIS SW$\downarrow$ surfaces do not appear to respond with changes in elevation along the transect (solid lines in Figs. 9c,d). This could be noteworthy as the major assumption of the elevation correction is that the satellite SW$\downarrow_t$ surfaces represent conditions at sea level. As the MODIS SW$\downarrow_t$ surfaces have a finer spatial resolution (1 km), they tend to display more variability along the radiation profiles. The profiles also reveal a potential problem with the radiative transfer–derived MODIS SW$\downarrow$ surfaces. Instead of radiation increasing with elevation, the MODIS SW$\downarrow$ surfaces show a significant drop in radiation at the top of the highest peak along the transect (Figs. 9c,d; approximately 200 m along transect). Since the highest elevation along the transect has the lowest radiation, the elevation correction does not appear to work correctly when applied to the MODIS SW$\downarrow$ surfaces. Similar to the NARR December profile, there is a considerable drop in the MODIS December SW$\downarrow_{te}$ after elevation correction (Fig. 9d). This is the result of modeling direct radiation as a fraction of S_0 in Eq. (6).

d. Topographic correction

It is difficult to validate the effect of topographic corrections with ground-measured data, as pyranometers are leveled to provide measurements of radiation on a horizontal plane. Thus to better understand the impact of topographic correction on the spatial structure of the radiation surfaces we opted to directly compare the NARR and MODIS total incoming radiation surfaces before (i.e., SW$\downarrow_t$) and after topographic correction [SW$\downarrow_{tet}$ output from topographic correction in section 3b(4)]. To explore the effect of topographic correction on the spatial structure of the radiation surfaces a series of semivariograms were constructed for a 190 000 km^2 mountainous region in central British Columbia (see Fig. 1 for location). The selected region has a strong southwest–northeast gradient in radiation, making it ideal for testing directional autocorrelation. Within the sample region, 10 000 randomly selected points were used to derive directional semivariograms from the NARR and MODIS July 2003 total incoming solar radiation surfaces both prior to (i.e., SW$\downarrow_t$) and after topographic correction (i.e., SW$\downarrow_{tet}$).

Figures 10a and 10c show that neither the 32-km NARR nor the 1-km MODIS July SW$\downarrow_t$ surfaces have enough spatial variation to cause a peak (or sill) in their respective semivariograms. This is primarily because solar radiation is a broad-scale phenomenon, especially when modeled at a monthly time step. Given the broad nature of radiation, it is not unlikely for samples to be similar even if taken from large distances away from one another (i.e., lag). After topographic correction however, both the NARR and MODIS SW$\downarrow_t$ surfaces show similar ranges ($\approx$1000 m) in spatial autocorrelation (Figs. 10b,d). This finding is in agreement with other studies that have shown that even at finer spatial resolutions (e.g., 30-m pixel resolution) most variation in solar radiation surfaces occurs within the first 1000 m (Dubayah 1994).

In addition to semivariograms, we also developed monthly scatterplots of NARR and MODIS total incoming solar radiation using a sample of 23 000 pixels distributed systematically over the PNW study area (Fig. 11). To minimize the difference in spatial resolution between the surfaces prior to topographic correction, we upscaled the 1-km MODIS SW$\downarrow_t$ surfaces to 32 km for comparison with the NARR SW$\downarrow_t$ surfaces. After topographically downscaling the 32-km NARR SW$\downarrow_t$ surfaces to 1 km, the graphs were replotted to highlight the effect topographic correction had on the radiation surfaces.

The topographic correction improved the correlation between the NARR and MODIS surfaces for all months in 2003 (statistics not presented). Winter, spring, and late fall correlations improved the most, and summer and early fall months (June–October) the least. Bias was improved in 8 of 12 months in 2003. Overall, topographic correction served to minimize the spatial and methodological differences that exist between the NARR and MODIS SW$\downarrow_t$ surfaces, making them more consistent for inclusion in broad-scale forest productivity models.

5. Discussion

Annually, the NARR and MODIS SW$\downarrow_t$ surfaces were in strong agreement with the ground measurements. Although on a monthly basis correlations varied, the NARR SW$\downarrow_t$ surfaces had equal or higher correlations
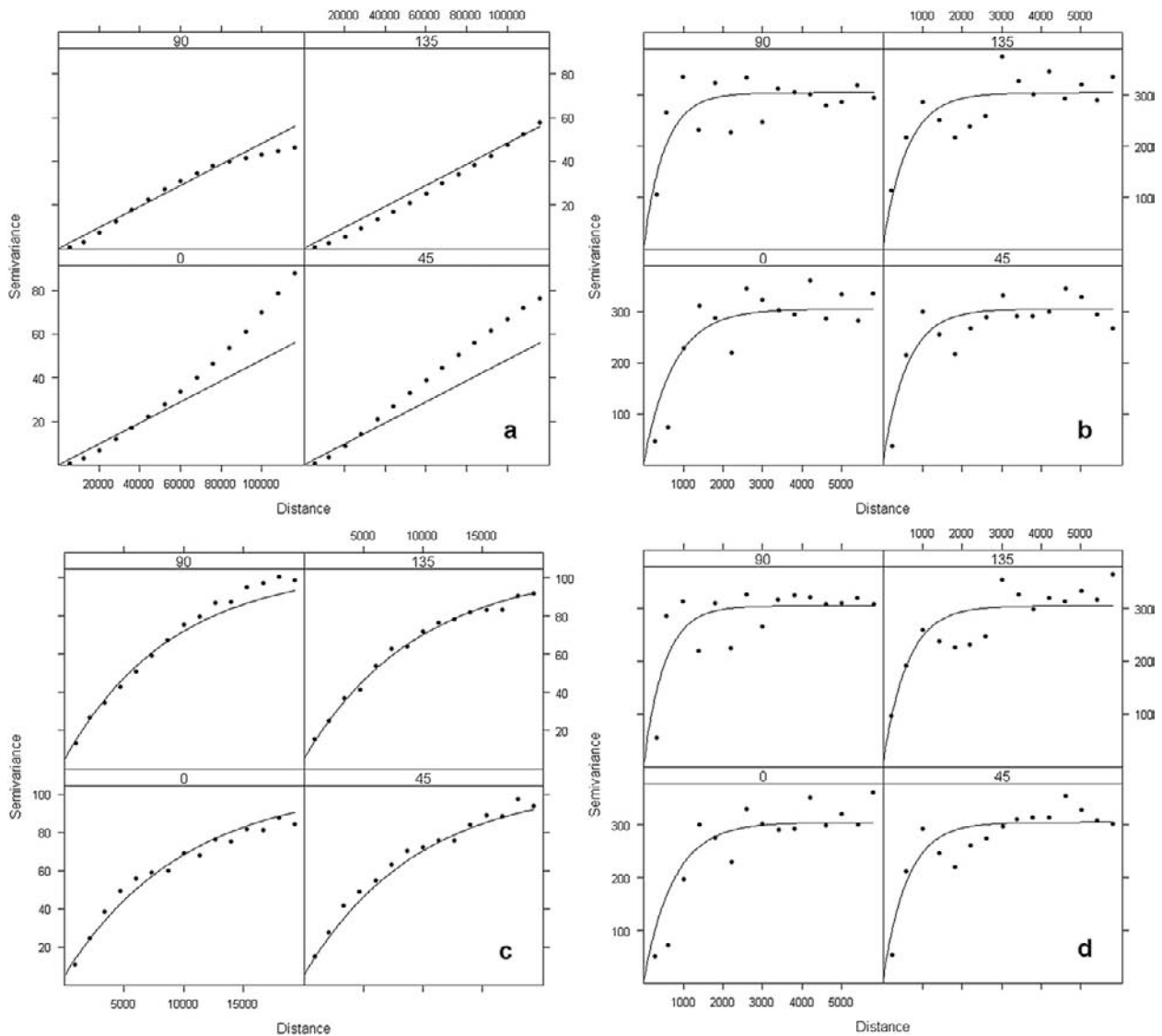
FIG. 10. Directional semivariograms based on July 2003 total incoming solar radiation from (a) NARR SW↓$_t$, (b) NARR SW↓$_{tet}$, (c) MODIS SW↓$_t$, and (d) MODIS SW↓$_{tet}$ surfaces. Direction: 0 = north, 45 = northeast, 90 = east, and 135 = southeast. Solid lines are best fits through the semivariance points.

than the MODIS SW↓$_t$ surfaces in all but one month in 2003. The annual bias observed in the original NARR SW↓$_t$ surfaces (35.13 W m^{-2}, min = 14.74 W m^{-2}, max = 57.65 W m^{-2}) was similar in magnitude to estimates reported by Berbery et al. (1999). The initial bias adjustment based on the annual relationship between the original NARR SW↓$_t$ surfaces and the ground data effectively minimized bias to 0.76 W m^{-2} ($\pm$10 W m^{-2}). Although the use of monthly equations would have likely yielded even less bias, the annual equation provided a quick and effective means of adjusting the NARR SW↓$_t$ surfaces.

When compared with the ground measurements, the NARR SW↓$_t$ surfaces had slightly higher correlations,

whereas the MODIS SW↓$_t$ surfaces exhibited less bias. On an annual basis, the NARR and MODIS SW↓$_t$ surfaces had similar relative error (average as percent relative to the mean). Both showed less error in the late spring, summer, and early fall when the atmosphere is relatively clear and the highest error in winter and late fall when cloud cover dominates the PNW region. Overall, despite methodological and spatial resolution differences, both the NARR and MODIS SW↓$_t$ surfaces effectively resolved the broad-scale monthly radiation patterns recorded by the ground data.

Annually the NARR and MODIS SW↓$_{df}$ surfaces were in relatively good agreement with ground data, although both tended to underpredict diffuse radiation when above

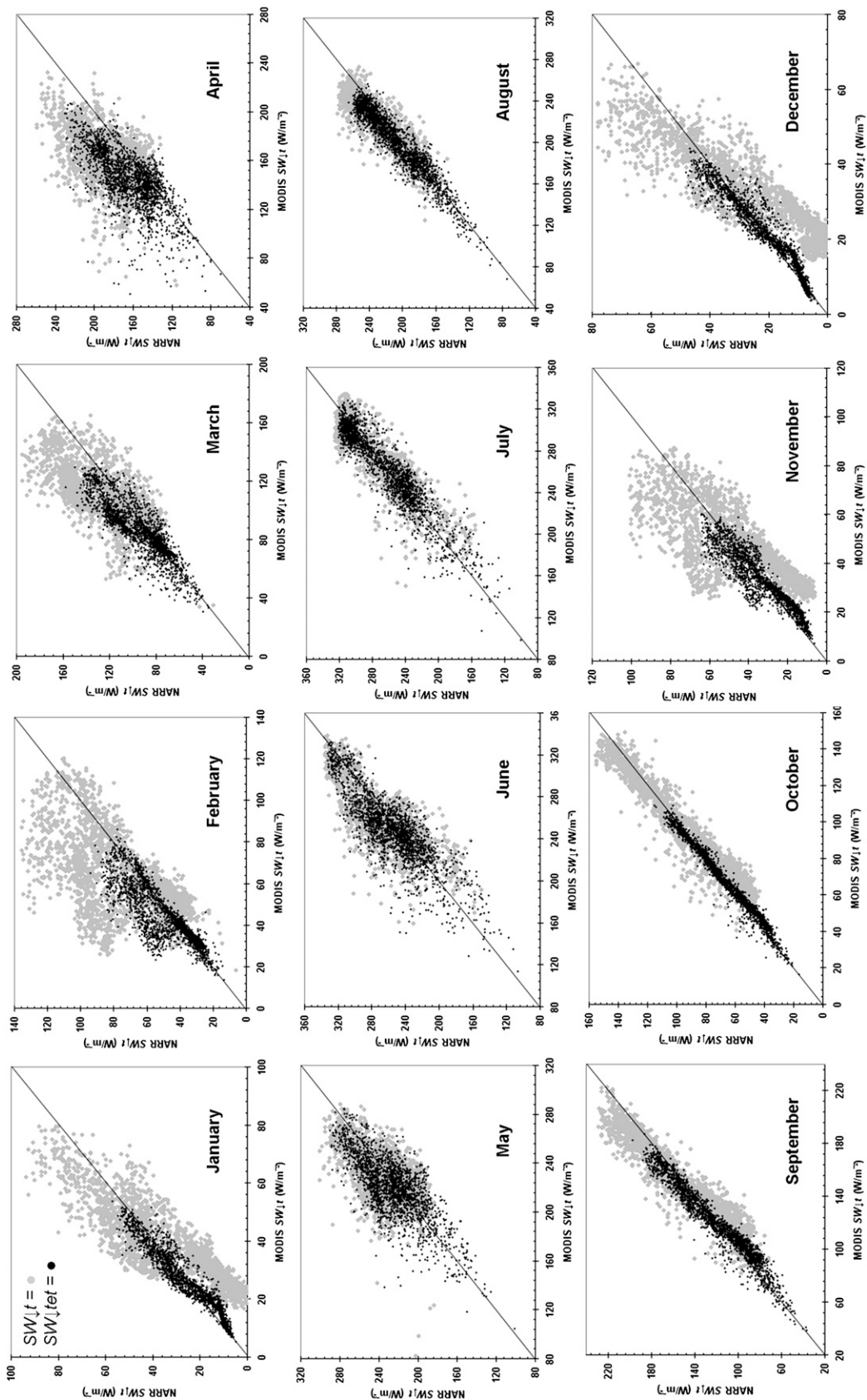FIG. 11. Scatterplots of NARR vs MODIS monthly average total incoming solar radiation (W m^{-2}) before (i.e., SW$\downarrow_t$ = gray symbols) and after (i.e., SW$\downarrow_{tet}$ = black symbols) topographic correction.

80 W m^{-2}. On a monthly basis, however, the correlations were weak, likely because of several months having virtually no correlation with the ground data. On a monthly basis, the NARR SW$\downarrow_{df}$ surfaces tended to have higher correlations with ground data, especially in late spring and summer months. Both the NARR and MODIS SW$\downarrow_{df}$ surfaces showed similar seasonal variations in bias, although NARR SW$\downarrow_{df}$ surfaces tended to be within ±10 W m^{-2}, while the MODIS SW$\downarrow_{t}$ surfaces were generally within ±20 W m^{-2} of the ground-measured data. Although monthly error was highly variable, the NARR SW$\downarrow_{df}$ surfaces tended to have less error than the MODIS SW$\downarrow_{df}$ surfaces. Overall, both the NARR and MODIS SW$\downarrow_{df}$ surfaces require additional improvement before being considered useful inputs to forest productivity models.

Elevation is broadly considered in the Eta forecasting model used to create the NARR SW$\downarrow_{t}$ surfaces. This broad-scale elevation effect was apparent in the response of the NARR SW$\downarrow$ surfaces across the elevation transect (solid lines in Figs. 9a,b). The elevation correction did seem to work properly in the summer profile, but not in the winter when transmittance (e.g., K_T) was low. In winter, direct radiation drops far below its partitioned value, as it was modeled in Eq. (6) as a very small fraction of S_0. This problem could be eliminated if the diffuse profile was adjusted for elevation effects and the direct profile was simply obtained by subtracting the elevation-corrected diffuse from total incoming radiation. Given the response of the NARR SW$\downarrow$ surfaces to elevation, it is questionable whether the elevation correction is necessary. The MODIS SW$\downarrow$ surfaces showed no visible signs of responding to changes in elevation prior to elevation correction. This is possibly in better agreement with the model assumption that satellite-based SW$\downarrow$ surfaces have no relationship with elevation (i.e., satellite estimates should represent conditions at sea level). The sharp drop in the radiation over the highest peak along the transect (Figs. 9c,d) is likely due to land cover confusion within the radiative transfer code used to create the MODIS SW$\downarrow$ surfaces. At high elevations, Cascade volcanoes are primarily made up of bare rock and ice. The highly reflective nature of these land cover surfaces could result in significant underestimation of surface radiation when utilizing a radiative transfer modeling approach. Once this problem is addressed, the MODIS SW$\downarrow$ surfaces might well respond more realistically to changes in elevation.

The topographic correction was effective in downscaling the 32-km NARR SW$\downarrow_{t}$ surfaces to 1 km. In doing so, the NARR and MODIS SW$\downarrow_{t}$ surfaces became much more similar in terms of correlation, bias, and spatial structure (Figs. 10 and 11). Increased consistency in SW$\downarrow$ surfaces, which resulted from topographic correction, should act to minimize errors in forest productivity models that use different solar radiation inputs (Zhao et al. 2006). Furthermore, our results suggest that forest productivity models that use uncorrected SW$\downarrow_{t}$ surface inputs could overestimate incoming solar radiation by as much as 25 (±12) W m^{-2} on north-facing slopes and 19 (±11) W m^{-2} on south-facing slopes. These average estimates were calculated across the full study area; thus the overestimation of incoming radiation for any one point on the landscape could actually be much higher depending on time of year and steepness of slope.

Overall, both the NARR and MODIS SW$\downarrow_{t}$ surfaces effectively captured the broad-scale radiation patterns recorded at the ground stations. Once corrected for initial bias, we found the NARR SW$\downarrow_{t}$ surfaces to be as accurate as higher–spatial resolution monthly average radiation surfaces derived from MODIS imagery. We note that several improvements have recently been made to the MODIS PAR product used in this paper. These improvements include the use of a visibility interpolation algorithm (Wang et al. 2009) for daily PAR integration and the implementation of an operational topographic correction procedure (Zheng et al. 2008) similar to the one presented here. These improvements to the MODIS algorithm are being incorporated into an operational effort to produce radiation surfaces of the global land surface. As radiation surface products become more readily available, additional validation efforts will be required. Alternately, more work is needed to improve methods for estimating diffuse radiation from total radiation. The topographic solar radiation model presented here was successfully modified to work with monthly average data, making operational correction of longer radiation time series a viable option. Direct comparison of NARR and MODIS SW$\downarrow_{t}$ surfaces provided a valuable example of how topographic correction can improve the consistency (i.e., higher correlation and lower bias) of radiation surfaces derived from different modeling frameworks. This improved similarity should help to minimize errors among forest productivity models that use different solar radiation inputs.

APPENDIX

Symbol Definitions

$\cos\theta_0$ Monthly average daytime cosine of the solar zenith angle

C_t Terrain configuration factor

$(\bar{d}/d)^2$ Monthly average Earth–sun distance

h Monthly average sunset hour angle (radians)

K_T Clearness index

M_z Fraction of unabsorbed exoatmospheric flux at elevation of each DEM grid cell

M_0 Fraction of unabsorbed exoatmospheric flux at reference height (sea level)

P_0 Atmospheric pressure at reference height (sea level)

P_j Atmospheric pressure at height of each DEM grid cell

P_{height} Air pressure at elevation of each DEM grid cell (bar)

PRR   Potential relative radiation (unitless)

P_{sealevel} Air pressure at reference height (sea level), (bar)

$\overline{R}_{\text{mod}}$ MODIS monthly average red surface reflectance

S_0 Monthly average exoatmospheric irradiance on a horizontal surface (W m^{-2})

SW↓   Incoming shortwave solar radiation (W m^{-2})

SW↓$_t$ Incoming monthly average total shortwave radiation (W m^{-2})

SW↓$_{te}$ Incoming monthly average total shortwave radiation on a horizontal surface at elevation of each DEM grid cell (W m^{-2})

SW↓$_{tet}$ Topographically corrected incoming monthly average total shortwave radiation (W m^{-2})

SW↓$_{df}$ Incoming monthly average diffuse radiation (W m^{-2})

SW↓$_{dfe}$ Incoming monthly average diffuse radiation received on a horizontal surface at elevation of each DEM grid cell (W m^{-2})

SW↓$_{dfet}$ Topographically corrected incoming monthly average diffuse radiation (W m^{-2})

SW↓$_{dr}$ Incoming monthly average direct radiation (W m^{-2})

SW↓$_{dre}$ Incoming monthly average direct radiation received on a horizontal surface at elevation of each DEM grid cell (W m^{-2})

SW↓$_{dret}$ Topographically corrected incoming monthly average direct radiation (W m^{-2})

SW↑$_{\text{ref}}$ Monthly average reflected radiation (W m^{-2})

T Monthly average total transmittance of the atmosphere

t_0 Optical depth at sea level

t_z Optical depth at elevation of each DEM grid cell

V_d Skyview factor

ϕ Latitude (radians)

δ Monthly average declination angle (radians)

REFERENCES

Alados, I., I. Foyo-Moreno, and L. Alados-Arboledas, 1996: Photosynthetically active radiation: Measurements and modelling. *Agric. For. Meteor.,* **78,** 121–131.

Babst, F., R. W. Mueller, and R. Hollman, 2008: Verification of NCEP reanalysis shortwave radiation with mesoscale remote sensing data. *IEEE Trans. Geosci. Remote Sens.,* **5,** 34–37.

Berbery, E. H., K. E. Mitchell, S. Benjamin, T. Smirnova, H. Ritchie, R. Hogue, and E. Radeva, 1999: Assessment of land-surface energy budgets from regional and global models. *J. Geophys. Res.,* **104,** 19 329–19 348.

Betts, A. K., S.-Y. Hong, and H.-L. Pan, 1996: Comparison of NCEP–NCAR reanalysis with 1987 FIFE data. *Mon. Wea. Rev.,* **124,** 1480–1498.

——, F. Chen, K. E. Mitchell, and Z. I. Janjić, 1997: Assessment of the land surface and boundary layer models in two operational versions of the NCEP Eta model using FIFE data. *Mon. Wea. Rev.,* **125,** 2896–2916.

Black, T. L., 1994: The new mesoscale Eta model: Description and forecast examples. *Wea. Forecasting,* **9,** 265–278.

Brodersen, C. R., T. C. Vogelmann, W. E. Williams, and H. L. Gorton, 2008: A new paradigm in leaf-level photosynthesis: Direct and diffuse lights are not equal. *Plant Cell Environ.,* **31,** 159–164.

Brotzge, J. A., 2004: A two-year comparison of the surface water and energy budgets between two OASIS sites and NCEP–NCAR reanalysis data. *J. Hydrometeor.,* **5,** 311–326.

COESA, 1976: U.S. Standard Atmosphere, 1976. NOAA, 227 pp.

Cohen, W. B., M. E. Harmon, D. O. Wallin, and M. Fiorella, 1996: Two decades of carbon flux from forests of the Pacific Northwest. *BioScience,* **46,** 836–844.

——, T. K. Maiersperger, S. T. Gower, and D. P. Turner, 2003: An improved strategy for regression of biophysical variables and Landsat ETM+ data. *Remote Sens. Environ.,* **84,** 561–571.

Coops, N. C., R. H. Waring, and J. B. Moncrieff, 2000: Estimating mean monthly incident solar radiation on horizontal and inclined slopes from mean monthly temperature extremes. *Int. J. Biometeor.,* **44,** 204–211.

Dozier, J., 1980: A clear-sky spectral solar radiation model for snow-covered mountainous terrain. *Water Resour. Res.,* **16,** 709–718.

——, 1989: Spectral signature of alpine snow cover from the Landsat Thematic Mapper. *Remote Sens. Environ.,* **28,** 9–22.

——, and J. Frew, 1990: Rapid calculation of terrain parameters for radiation modeling from digital elevation data. *IEEE Trans. Geosci. Remote Sens.,* **28,** 963–969.

Dubayah, R., 1992: Estimating net solar radiation using Landsat Thematic Mapper and digital elevation data. *Water Resour. Res.,* **28,** 2469–2484.

——, 1994: Modeling a solar radiation topoclimatology for the Rio Grande river basin. *J. Veg. Sci.,* **5,** 627–640.

——, and V. van Katwijk, 1992: The topographic distribution of annual incoming solar radiation in the Rio Grande River basin. *Geophys. Res. Lett.,* **19,** 2231–2234.

——, and P. M. Rich, 1995: Topographic solar radiation models for GIS. *Int. J. Geogr. Inf. Syst.,* **9,** 405–419.

——, and S. Loechel, 1997: Modeling topographic solar radiation using GOES data. *J. Appl. Meteor.,* **36,** 141–154.

Duffie, J. A., and W. A. Beckman, 1974: *Solar Engineering of Thermal Processes.* John Wiley and Sons, 386 pp.

Erbs, D. G., S. A. Klein, and J. A. Duffie, 1982: Estimation of the diffuse radiation fraction for hourly, daily and monthly-average global radiation. *Sol. Energy,* **28,** 293–302.

Frew, J. E., 1991: The image processing workbench. Ph.D. thesis, University of California, Santa Barbara, 412 pp.

Gu, L. H., D. D. Baldocchi, S. B. Verma, T. A. Black, T. Vesala, E. M. Falge, and P. R. Dowty, 2002: Advantages of diffuse radiation for terrestrial ecosystem productivity. *J. Geophys. Res.,* **107,** D64050, doi:10.1029/2001JD001242.

Gupta, S. K., D. P. Kratz, P. W. Stackhouse Jr., and A. C. Wilber, 2001: The Langley parameterized shortwave algorithm (LPSA) for surface radiation budget studies version 1. NASA/TP-2001-211272, 26 pp.

Hamann, A., and T. L. Wang, 2004: Models of climatic normals for genecology and climate change studies in British Columbia. *Agric. For. Meteor.,* **128,** 211–221.

Kalnay, E., and Coauthors, 1996: The NCEP/NCAR 40-Year Reanalysis Project. *Bull. Amer. Meteor. Soc.,* **77,** 437–471.

Katsoulis, B. D., 1991: A comparison of several diffuse solar radiation models for Greece. *Theor. Appl. Climatol.,* **44,** 181–186.

Kistler, R., and Coauthors, 2001: The NCEP–NCAR 50-Year Reanalysis: Monthly means CD-ROM and documentation. *Bull. Amer. Meteor. Soc.,* **82,** 247–267.

Landsberg, J. J., and R. H. Waring, 1997: A generalized model of forest productivity using simplified concepts of radiation-use efficiency, carbon balance and partitioning. *For. Ecol. Manage.,* **95,** 209–228.

LeBaron, B. A., and I. Dirmhirn, 1983: Strengths and limitations of the Liu and Jordan model to determine diffuse from global irradiance. *Sol. Energy,* **31,** 167–172.

Liang, S., T. Zheng, R. Liu, H. Fang, S.-C. Tsay, and S. W. Running, 2006: Estimation of incident photosynthetically active radiation from Moderate Resolution Imaging Spectrometer data. *J. Geophys. Res.,* **111,** D15208, doi:10.1029/2005JD006730.

Liu, B. Y. H., and R. C. Jordan, 1960: The interrelationship and characteristic distribution of direct, diffuse and total solar radiation. *Sol. Energy,* **4,** 1–19.

Liu, R., S. Liang, H. He, J. Liu, and T. Zheng, 2008: Mapping incident photosynthetically active radiation from MODIS data over China. *Remote Sens. Environ.,* **112,** 998–1009.

Lowry, W. P., 1980: Direct and diffuse solar radiation: Variations with atmospheric turbidity and altitude. IES Research Rep. 6, UILU-IES 800006, University of Illinois at Urbana–Champaign, 190 pp.

Meek, D. W., J. L. Hatfield, T. A. Howell, S. B. Idso, and R. J. Reginato, 1984: A generalized relationship between photosynthetically active radiation and solar radiation. *Agron. J.,* **76,** 939–945.

Mittelstadt, J., 1998: The Eta-32 model. Western Region Tech. Attachment 98-03, NWS. [Available online at http://www.wrh.noaa.gov/wrh/98TAs/9803/index.html.]

Oliveira, A. P., J. F. Escobedo, A. J. Machado, and J. Soares, 2002: Correlation models of diffuse solar-radiation applied to the city of São Paulo, Brazil. *Appl. Energy,* **71,** 59–73.

Perez, R., P. Ineichen, K. Moore, M. Kmiecik, C. Chain, R. George, and F. Vignola, 2002: A new operational model for satellite-derived irradiances: Description and validation. *Sol. Energy,* **73,** 307–317.

Pierce, K. B., T. Lookingbill, and D. Urban, 2005: A simple method for estimating potential relative radiation (PRR) for landscape-scale vegetation analysis. *Landscape Ecol.,* **20,** 137–147.

Qian, T., A. Dai, K. E. Trenberth, and K. W. Oleson, 2006: Simulation of global and land surface conditions from 1948 to 2002: I. Forcing data and evaluations. *J. Hydrometeor.,* **7,** 953–975.

Running, S. W., R. R. Nemani, F. A. Heinsch, M. S. Zhao, M. Reeves, and H. Hashimoto, 2004: A continuous satellite derived measure of global terrestrial primary production. *BioScience,* **54,** 547–560.

Sellers, W. D., 1965: *Physical Climatology.* University of Chicago Press, 272 pp.

Serreze, M. C., and C. M. Hurst, 2000: Representation of mean Arctic precipitation from NCEP–NCAR and ERA reanalyses. *J. Climate,* **13,** 182–201.

Sheffield, J., G. Goteti, and E. F. Wood, 2006: Development of a 50-year high-resolution global dataset of meteorological forcings for land surface modeling. *J. Climate,* **19,** 3088–3111.

Thornton, P. E., and S. W. Running, 2000: An improved algorithm for estimating incident daily solar radiation from measurements of temperature, humidity and precipitation. *Agric. For. Meteor.,* **93,** 211–228.

——, and Coauthors, 2002: Modeling and measuring the effects of disturbance history and climate on carbon and water budgets in evergreen needleleaf forests. *Agric. For. Meteor.,* **113,** 185–222.

Trenberth, K. E., and C. J. Guillemot, 1998: Evaluation of the atmospheric moisture and hydrologic cycle in the NCEP/NCAR reanalyses. *Climate Dyn.,* **14,** 213–231.

Turner, D. P., M. Guzy, M. A. Lefsky, W. D. Ritts, S. Van Tuyl, and B. E. Law, 2004: Monitoring forest carbon sequestration with remote sensing and carbon cycle modeling. *Environ. Manage.,* **33,** 457–466.

Van Laake, P. E., and G. A. Sanchez-Azofeifa, 2004: Simplified atmospheric radiative transfer modeling for estimating incident PAR using MODIS atmosphere products. *Remote Sens. Environ.,* **91,** 98–113.

Vignola, F., J. Domingo, and D. K. McDaniels, 1996: Comparisons with a rotating shadowband pyranometer. *Proc. 1996 American Solar Energy Society,* Asheville, NC, American Solar Energy Society, 229–236.

Wang, D., S. Liang, R. Liu, and T. Zheng, 2009: Estimation of daily-integrated PAR from sparse satellite observations: Comparison of temporal scaling methods. *Int. J. Remote Sens.,* in press.

Wang, T. L., A. Hamann, D. L. Spittlehouse, and S. N. Aitken, 2006: Development of scale-free climate data for western Canada for use in resource management. *Int. J. Climatol.,* **26,** 383–397.

Yang, S., Y. Hou, A. Miller, and K. Campana, 1999: Evaluation of the earth radiation budget in NCEP–NCAR reanalysis with ERBE. *J. Climate,* **12,** 477–493.

Zhao, M., S. W. Running, and R. R. Nemani, 2006: Sensitivity of Moderate Resolution Imaging Spectroradiometer (MODIS) terrestrial primary production to the accuracy of meteorological reanalyses. *J. Geophys. Res.,* **111,** G01002, doi:10.1029/2004JG000004.

Zhao, Q., T. L. Black, and M. E. Baldwin, 1997: Implementation of the cloud prediction scheme in the Eta model at NCEP. *Wea. Forecasting,* **12,** 697–712.

Zheng, T., S. Liang, and K. Wang, 2008: Estimation of incident photosynthetically active radiation from GOES visible imagery. *J. Appl. Meteor. Climatol.,* **47,** 853–868.